Research

Check for updates

Author for correspondence:
Massimo Ruzzene
e-mail: ruzzene@gatech.edu

A study of deformation localization in nonlinear elastic square lattices under compression

Raj Kumar Pal[1], Federico Bonetto[2], Luca Dieci[2] and Massimo Ruzzene[1,3]

[1]School of Aerospace Engineering, [2]School of Mathematics, and [3]School of Mechanical Engineering, Georgia Institute of Technology, Atlanta, GA 30332, USA

MR, 0000-0002-1502-2160

The paper investigates localized deformation patterns resulting from the onset of instabilities in lattice structures. The study is motivated by previous observations on discrete hexagonal lattices, where a variety of localized deformations were found depending on loading configuration, lattice parameters and boundary conditions. These studies are conducted on other lattice structures, with the objective of identifying and investigating minimal models that exhibit localization, hysteresis and path-dependent behaviour. To this end, we first consider a two-dimensional square lattice consisting of point masses connected by in-plane axial springs and vertical ground springs, which may be considered as a discrete description of an elastic membrane supported by an elastic substrate. Results illustrate that, depending on the relative values of the spring constants, the lattice exhibits in-plane or out-of-plane instabilities leading to localized deformations. This model is further simplified by considering the one-dimensional case of a spring–mass chain sitting on an elastic foundation. A bifurcation analysis of this lattice identifies the stable and unstable branches and sheds light on the mechanism of transition from affine deformation to global or diffuse deformation to localized deformation. Finally, the lattice is further reduced to a minimal four-mass model, which exhibits a deformation qualitatively similar to that in the central part of a longer chain. In contrast to the widespread assumption that localization is induced

by defects or imperfections in a structure, this work illustrates that such phenomena can arise in perfect lattices as a consequence of the mode shapes at the bifurcation points.

This article is part of the theme issue 'Nonlinear energy transfer in dynamical and acoustical systems'.

1. Introduction

Localized deformations resulting from instabilities arise naturally in a wide range of physical systems, and across multiple length scales. Manifestations include plastic twinning in metals [1], localized buckling of epithelial cells in biological media [2] and chevron folds in rocks [3], among others. The study of instabilities, both at the microstructural scale in materials and at the macroscopic structural level, is an area of renewed interest, and a timely research topic. Several studies have focused on exploiting the formation of patterns resulting from instabilities in engineered materials and structures to enable a variety of functionalities that are useful to applications ranging from flexible electronics to architected adaptive materials [4]. Instabilities and the ensuing pattern formations, or topological changes, for example, govern phase transitions in materials such as shape memory alloys [5] and attempts have been made at replicating similar principles in structural components. Extensive research has also been devoted to the study of instabilities in thin films on soft substrates [6,7], periodic composites [8] and lattices [9–11]. Relevant examples include the investigation of global pattern formation in periodic composites and lattices [12], and the onset of herringbone patterns in compressed thin films [13]. More recently, Bertoldi & Boyce [14] demonstrated how instabilities in soft polymers induce changes in the frequency band structure of periodic phononic systems, while Pal *et al.* [15,16] investigated the static and dynamic properties of hexagonal lattices and demonstrated that instabilities can lead to the surface confinement of elastic waves. Engineered defect distributions that induce desired deformation patterns in thin shells have been investigated in [17], where the onset of instabilities is shown to be associated with the breaking of discrete lattice translational symmetry and can be predicted by a phonon stability analysis on a unit cell.

Of particular interest to the present study is the investigation of localized deformations associated with the onset of instabilities. Methodologies for the prediction and design of localized patterns are the objectives of numerous studies and are considered open challenges towards the understanding of failure as well as the engineering of desired interfaces that act as tunable elastic waveguides. The investigation of localization resulting from post-buckling in lattices and periodic media is presented, for example, in [15,18]. Although localization in continuous media, which manifests as discontinuous strain distributions, is typically assessed by examining the loss of ellipticity in the Hessian of the strain energy [19], its relation to the microstructure and the effect of the macroscopic geometry, including boundary conditions, remain elusive. Indeed, in contrast to a phonon stability analysis on a single unit cell for identifying diffuse instabilities, no such recipe exists for localization. Several studies [20,21] have demonstrated, both numerically and experimentally, how buckling at the microstructural level evolves into localized deformations. In this context, notable are the works of Papka & Kyriakides [22,23], who investigated the crushing of honeycomb cellular lattices under a variety of loading conditions. More recently, d'Avila *et al.* [24] have demonstrated that the onset of localization in a periodic composite depends on the effective tangent stiffness of the composite and occurs only if this stiffness in the loading direction is negative. There have also been studies on localized vibration modes called intrinsically localized modes or discrete breathers, where localization arises as a consequence of discreteness and nonlinear interactions [25,26].

The current study is motivated by the observation of localized deformation patterns following the onset of instabilities in discrete, hexagonal lattices [15]. Notwithstanding the consideration of an idealized model free from defects and imperfections, these deformations are observed to occur as a result of the presence of nonlinearities corresponding to large displacements.
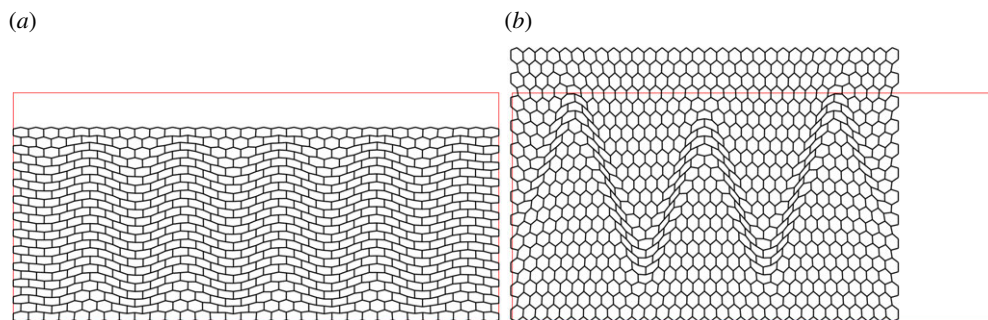
(a)   (b)

Figure 1. Deformed configurations having different localization patterns for different boundary conditions. (*a*) Biaxial loading with displacement prescribed on all boundary nodes. (*b*) Compression prescribed on horizontal direction and periodic conditions along vertical boundary nodes. (Online version in colour.)

Some of the localized deformation patterns observed in [15] are summarized here. Consider a hexagonal lattice, which consists of point masses connected by linear longitudinal springs, and includes angular springs that oppose the change in angle between neighbouring springs [15,16]. The lattice is constrained to deform in the x, y plane and undergoes large displacements resulting from the imposed set of displacements on the boundary. Figure 1*a* illustrates the lattice deformation corresponding to an imposed vertical displacement on the boundary. As the imposed displacement is progressively increased, the deformation evolves from being initially affine (linear in x and y) to subsequently achieving globally diffuse patterns. By contrast, figure 1*b* displays the case of a biaxial loading corresponding to imposed displacements along both the horizontal and vertical directions. The resulting deformed configuration is characterized by a localized deformation along a 'zig-zag' interface.

This example illustrates how instabilities in lattices leading to localized deformations or diffuse pattern formation depend on several factors, including lattice geometry, material parameters, boundary and loading conditions. Elucidating the interplay between these factors is a daunting challenge and is the subject of ongoing investigations. To address some of these questions, this paper focuses on progressively simpler lattices with the objective of identifying configurations that are characterized by localized deformations and may provide useful insight into the most relevant parameters that govern the behaviour of interest. An overview of the considered lattice configurations is shown in figure 2, which presents an elastically supported square lattice capable of both in-plane and out-of-plane motion (figure 2*a*). The dimensionality of this problem is reduced by extracting the single lattice strip shown in figure 2*b*, which then leads to the elementary case of the elastically supported one-dimensional (1D) spring–mass chain shown in figure 2*c*. The thin lines in figure 2 describe longitudinal springs that provide a restoring force aligned with the spring itself and proportional to the relative displacements of the two nodes it connects. The onset of localized deformation is initially based on observation of the deformed equilibrium configurations, which are evaluated through a Newton–Raphson procedure. For the low-dimensional cases of figure 2*b,c*, a linear bifurcation analysis and the application of a shooting method support the interpretation of the observed solutions, the prediction of stability characteristics, the evolution of the equilibrium deformed configurations with applied strain as well as the evaluation of loading path-dependent or hysteresis behaviours. A rich set of equilibrium solutions are illustrated which evolve from diffuse patterns to strongly localized ones. We remark that the transition and localization which we observe are not trivial. There is a vast literature on various physical models that show a variety of instabilities, including folds, crevices and wrinkles (e.g. [7] and subsequent papers citing this paper). Currently, there is a lack of understanding on the mechanics leading to symmetry-breaking transitions that lead to these deformations (the review paper [27] highlights some related challenges). The current work provides a simple model which may form the basis to understand such complex phenomena.
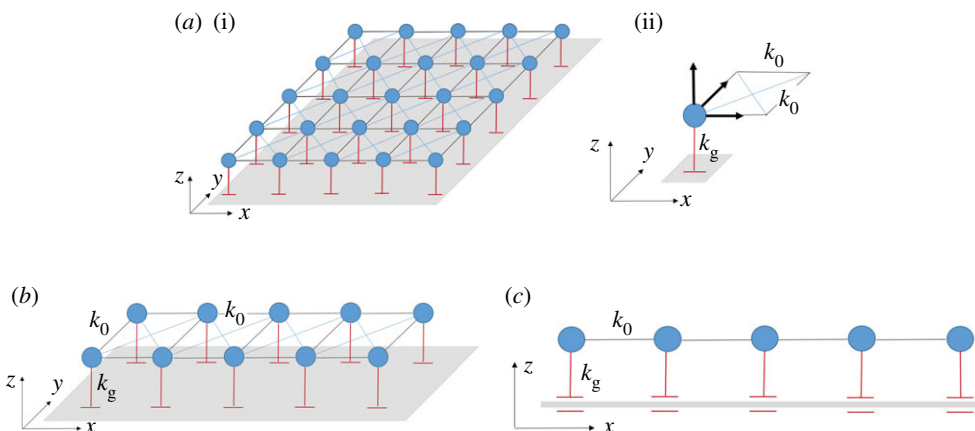
4

rsta.royalsocietypublishing.org *Phil. Trans. R. Soc. A* **376**: 20170140

Figure 2. Summary of discrete lattices considered for observation and analysis of instability-induced localization: (*a*) square lattice with ground springs (i) and detail of unit cell (ii), (*b*) 1D square lattice strip and (*c*) 1D spring–mass chain. (Online version in colour.)

The paper is organized as follows. Following this introduction, §2 presents two distinct kinds of instability that arise in square lattices interacting with ground springs: a localized deformation and a globally uniform pattern. Next, §3 investigates this localized deformation in an analogous 1D lattice using a combination of numerical simulations and bifurcation analysis. Finally, the conclusions of this work are summarized in §4.

2. Square lattice model

Let us consider a square lattice of $N \times M$ nodes, that is $(N - 1) \times (M - 1)$ unit cells, which includes point masses at the nodes and three types of springs connecting them. This lattice model is inspired by a membrane on an elastic foundation with point masses embedded in a square lattice network and undergoing small strains. The lattice may be considered as a discrete version of this structure. Each point mass has three translational degrees of freedom and can move in three spatial dimensions. The diagonal springs and the springs connecting nearest neighbours both have stiffness k_0. There is a ground spring of stiffness k_g, which resists motion in the out-of-plane z-direction. The quasi-static behaviour of a lattice of a given dimension is governed by a single non-dimensional stiffness parameter, $\gamma = k_g/k_0$. In all the subsequent calculations in this work, we investigate the behaviour of a lattice under uniaxial compression. Both the in-plane displacement components are prescribed at all the boundary nodes corresponding to this uniaxial strain, while the out-of-plane displacement component is free at all the nodes. Note that, although additional effects like bending energy may come into play in a real membrane undergoing large deformations, we only consider the above interactions here, as our objective is to understand the mechanism of transition from diffuse to localized deformations.

(a) In-plane and out-of-plane instability

We first investigate the quasi-static behaviour of this lattice under uniaxial compression along the x-direction with the strain denoted by δ_x. To this end, we conduct numerical simulations to determine the deformed configuration by increasing the strain incrementally from the undeformed configuration. At each strain level, the equilibrium configuration is obtained by minimizing the potential energy E of the lattice subject to the appropriate boundary conditions.

5

rsta.royalsocietypublishing.org   Phil. Trans. R. Soc. A **376**: 20170140

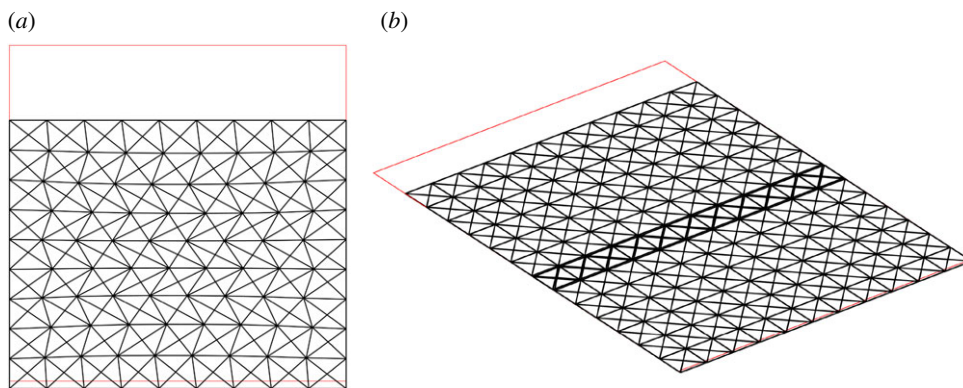(a)   (b)

Figure 3. Two kinds of instabilities in square lattices subjected to compression. (a) The deformation is in-plane and globally uniform at high stiffness parameter $\gamma = 1.0$, in contrast to (b) the out-of-plane and localized deformation at low $\gamma = 0.1$. (Online version in colour.)

The problem may be expressed as

$$
\begin{aligned}
\underset{\mathbf{X}}{\text{minimize}} \quad E(\mathbf{X}) = \frac{k_0}{2} \sum_{m=1}^{M-1} \sum_{n=1}^{N-1} & [(\|\mathbf{x}_{m,n} - \mathbf{x}_{m+1,n}\| - a)^2 + (\|\mathbf{x}_{m,n} - \mathbf{x}_{m,n+1}\| - a)^2 \\
& + (\|\mathbf{x}_{m,n} - \mathbf{x}_{m+1,n+1}\| - \sqrt{2}a)^2 + (\|\mathbf{x}_{m+1,n} - \mathbf{x}_{m,n+1}\| - \sqrt{2}a)^2] \\
& + \frac{k_g}{2} \sum_{m=1}^{M} \sum_{N=1}^{N} z_p^2 \\
\text{subject to} \quad x_q = (1 + \delta_x)X_q, & \quad y_q = 0, \quad q = 1, \ldots, N_b, \\
z_q = 0, & \quad q = 1, \ldots N_c.
\end{aligned}
\tag{2.1}
$$

Here N_b is the total number of boundary nodes, N_c is the number of nodes on the boundary along the y-direction, while (X_p, Y_p, Z_p) and $\mathbf{x}_p = (x_p, y_p, z_p)$ denote, respectively, the undeformed and deformed positions of node p and $\mathbf{X} = (\mathbf{x}_{1,1}, \mathbf{x}_{1,2}, \ldots, \mathbf{x}_{M,N})$. Finally, a is the distance between nearest-neighbour masses in the lattice.

Figure 3 illustrates the typical deformation field for two values of stiffness parameter γ. The two chosen γ values are representative of the behaviour of lattices with high and low γ. Figure 3a displays the in-plane deformation field when $\gamma = 1.0$. The out-of-plane displacement is zero and a globally diffuse pattern forms after the onset of an instability. The displacement field is affine for small strains δ near the undeformed configuration. This range of δ may be determined numerically using a procedure similar to the stability analysis presented later in §3b. With increasing strain, this affine solution loses stability, leading to the evolution of globally diffuse patterns with a wavelength of two unit cells along the loading direction and uniform along the transverse in-plane direction. We remark here that this deformation mode arises as a bifurcation since the affine solution satisfies the equilibrium equations. Figure 3b displays the deformation field for a square lattice with a lower stiffness parameter value $\gamma = 0.1$. Here the deformation happens along the out-of-plane direction too and leads to a localization which consists of one layer of the lattice folding over its adjacent layer. We observe that the deformation field is essentially two-dimensional, with no displacement in the transverse in-plane direction (y). Thus, we see that the patterns that form after the onset of a bifurcation depend on the material property, stiffness parameter γ in this case, and it can range from globally diffuse patterns to localized folding behaviour. We remark here that the folding after the localized deformation is a purely mathematical solution and may not always have physical relevance. In particular, other
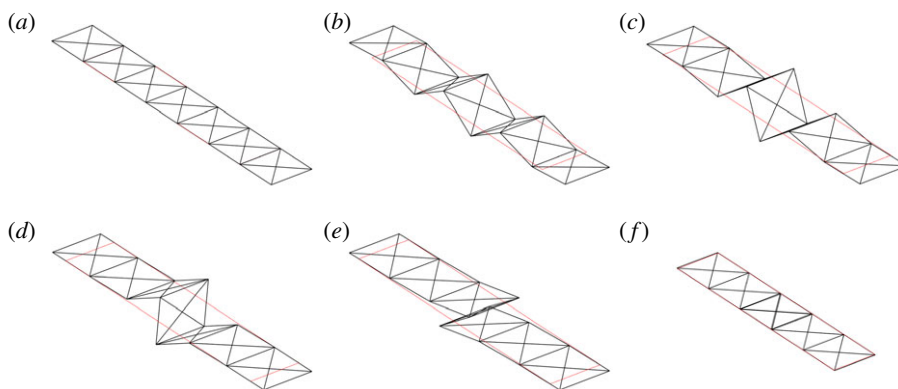
Figure 4. Snapshots of the folding transition process from the fully expanded and undeformed configuration (*a*) to the folded configuration (*f*), $\gamma = 0.1$. The process involves two distinct bifurcations, with the vertical deformation first increasing globally and then getting localized at the centre as the lattice is compressed. (Online version in colour.)

nonlinear effects, not considered here, may become relevant at this stage. Our focus in this work is to understand the transition from affine to global to localized deformations.

(b) Deformation sequence leading to localization

Let us examine the sequence of deformations that result in a localized folding pattern in a lattice with $\gamma = 0.1$. Since there is no displacement in the transverse in-plane direction, we consider a single strip of the square lattice with $N \times M = 2 \times 8$ nodes. Figure 4 illustrates the sequence of deformations as this lattice is subjected to a uniaxial compression. For small strains close to the undeformed configuration, the deformation field is affine and there is no out-of-plane displacement. As the strain increases, this affine solution becomes unstable and the lattice deforms out of plane in a zig-zag manner (figure 4*b*). The out-of-plane displacement is maximum at the centre and decreases away from it. As the strain increases further (figure 4*c*), the out-of-plane displacement increases for the centre nodes, while it decreases for nodes away from the centre. The out-of-plane displacement becomes localized at the two centre nodes of the lattice and it decreases rapidly to zero away from these nodes. As the strain increases, the centre square folds over (figure 4*e*–*f*), thereby resulting in a localized zone. Note that this localized deformation field will have zero-energy at a strain level $\delta = -2/(M-1) \approx -0.29$ when all the axial springs are unstretched and the out of plane displacement is zero. The existence of multiple zero-energy states (undeformed and folded configurations) implies that the potential energy is not quasi-convex. It also points to the existence of negative stiffness regions and the possibility of this lattice to exhibit hysteresis. A negative effective stiffness results in a snap-through type behaviour as the lattice transitions from the unfolded to the folded configuration or vice versa. We examine this rich set of behaviours arising due to this localized solution in the next section using a 1D model which turns out to be quite adequate for our purposes.

3. Chain on elastic support

To understand the mechanism of the snap-through behaviour during localization, let us further simplify the square lattice and consider an equivalent 1D model obtained by taking one section of the square lattice deprived of the diagonal springs. Figure 5 displays a schematic of the considered lattice model. There are N nodes along a strip indexed from 1 to N. The potential energy E of the

7

rsta.royalsocietypublishing.org   *Phil. Trans. R. Soc. A* **376**: 20170140
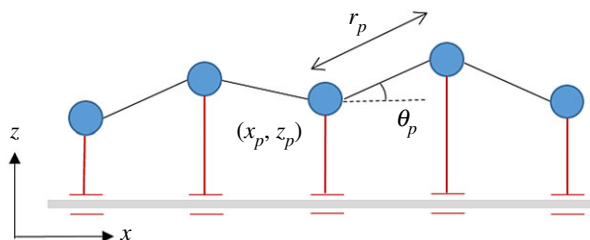
Figure 5. Schematic of a 1D lattice model, with point masses at the nodes interacting with nearest-neighbour horizontal springs and vertical ground springs. Each mass has two degrees of freedom and can move in the x–z plane. (Online version in colour.)
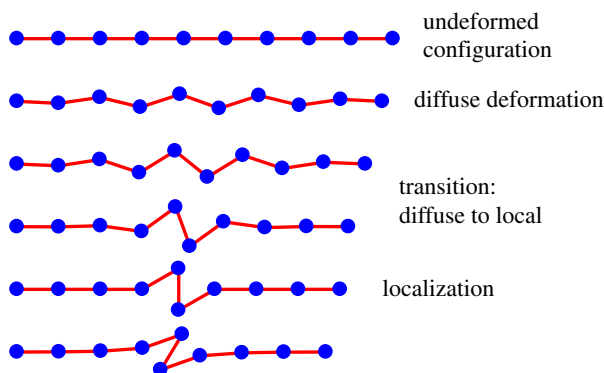

Figure 6. Sequence of deformed configurations as the lattice transitions from the undeformed to the localized deformation configuration. (Online version in colour.)

lattice may be written as

$$E(\mathbf{X}) = \sum_{i=1}^{N} \frac{k_{\mathrm{g}}}{2} z_i^2 + \sum_{i=1}^{N-1} \frac{k_0}{2} (\|x_i - x_{i+1}\| - a)^2, \qquad (3.1)$$

where $x_i = (x_i, z_i)$ and $\mathbf{X} = (x_1, x_2, \ldots, x_N)$. Here we can assume that the undeformed axial springs have unit length ($a = 1$). Minimizing this energy subject to the boundary conditions yields the equilibrium configuration. We illustrate the typical displacement response history as the folding transition happens in this model (figure 6).

We first conduct numerical simulations on a lattice of $N = 10$ masses by subjecting it to both a compressive strain from the unfolded configuration and a tensile strain from the folded configuration. For both cases, we denote the strain by δ, measuring it from the reference unfolded configuration. The numerical simulations are again conducted using a Newton–Raphson solver. This numerical solver based on incrementally applying strain faces convergence issues in the presence of instabilities and bifurcations. To overcome these limitations, we develop alternative techniques in §3c.

(a) Folding behaviour

This 1D model also undergoes a folding-based localization and we will analyse the deformation process leading to this localization in detail. In all our subsequent calculations, we consider a chain of 10 point masses (nodes) connected by axial springs of stiffness k_0. Similar to the square lattice, each mass is also connected to the ground by a spring of stiffness k_{g} and the quasi-static behaviour is then governed by the non-dimensional stiffness parameter $\gamma = k_{\mathrm{g}}/k_0$. The

8

rsta.royalsocietypublishing.org Phil. Trans. R. Soc. A **376**: 20170140
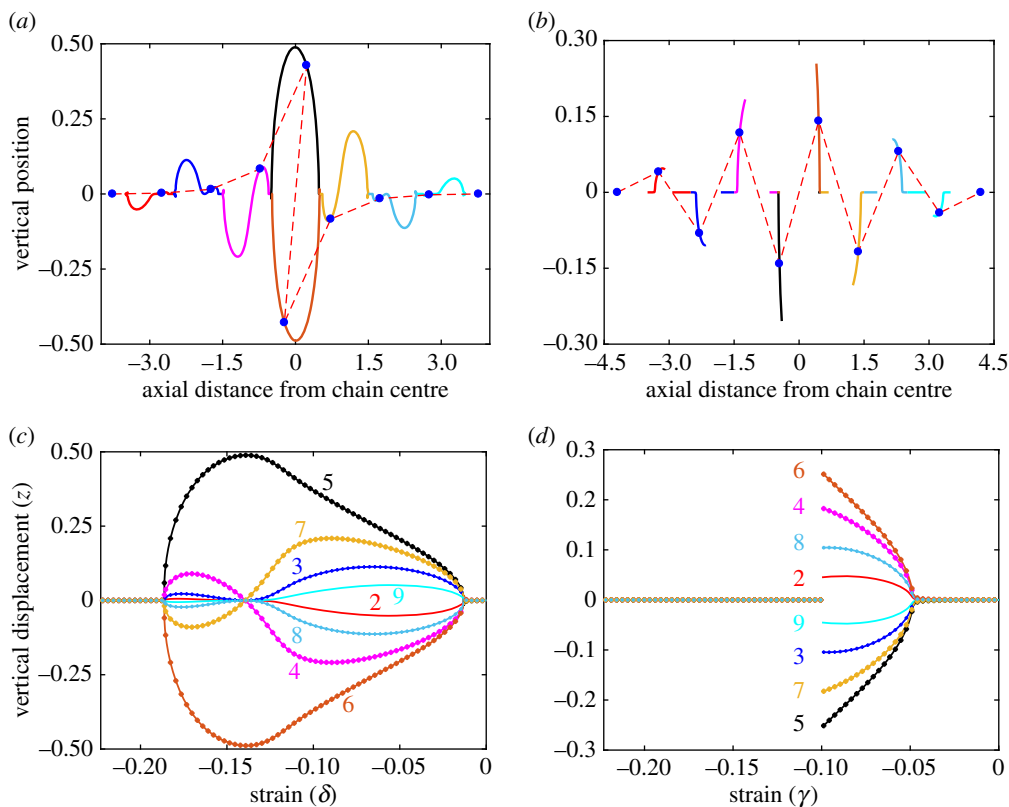

Figure 7. Vertical displacement of the nodes ($i = 1$ to 9) as the lattice is pulled from the folded configuration. Two bifurcation points are observed at low stiffness parameter $\gamma = 0.05$ (a,c), while a single bifurcation and a jump in displacement is obtained at high $\gamma = 0.2$ (b,d). (Online version in colour.)

chain starts from $x = 0$ and the undeformed lattice spans from $x_1 = 0$ to $x_{10} = 9$. This is referred to as the unfolded configuration. The first mass is kept fixed while the last mass is subjected to a compressive displacement. The two end masses are also restricted from moving vertically ($z_1 = z_{10} = 0$). As the prescribed compressive displacement increases, the lattice folds at the centre and now spans from $x_1 = 0$ to $x_{10} = 7$. This is referred to as the folded configuration. Thus, we have that $\delta = 0$ for the unfolded configuration while $\delta = -2/9$ for the folded one. Figure 6 displays snapshots of the deformed lattice as it deforms from one configuration to the other. We will analyse the quasi-static response of the lattice as it deforms from the folded to the unfolded configuration and vice versa.

Figure 7 displays the vertical displacement of the nodes as this lattice is subjected to a tensile strain from the folded configuration. Note that the lattice in the initial configuration spans from $x_1 = 0$ to $x_{10} = 7$ in the axial direction. As the lattice is pulled from both ends, it reaches a final unfolded and undeformed configuration ranging from 0 to 9. The horizontal and vertical axes show, respectively, the compressive strain δ measured from the reference unfolded configuration and the vertical displacement of all the nodes in between. Figure 7c displays the displacements for stiffness parameter $\gamma = 0.1$. At small displacements from the initial configuration, the axial displacement field is affine in the lattice and the vertical displacement is zero. At around $\delta = -0.187$, there is an instability and the lattice deforms out of plane, thereby initiating the unfolding process. The vertical displacement decreases away from the centre nodes and it increases with increasing tensile strain near the bifurcation point. The nodes to the right of the centre spring have a positive vertical displacement while the corresponding nodes to the left have an equal and opposite vertical displacement.

As the tensile strain increases, the vertical displacement of the nodes away from the centre decrease to zero at around $\delta = -0.139$. Beyond this point, the shape of the displacement field changes as the vertical displacements of adjacent nodes alternate in sign. They first increase and then decrease in magnitude, reaching a zero value at around $\delta = -0.011$. Beyond this point, the displacement field is affine in the axial direction and has no vertical component. This deformation mode corresponds to uniform compression of the lattice from the unfolded and undeformed position, which is attained at $x_{10} = 9$. We thus see two distinct mode shapes arising from the onset of two bifurcation points as the lattice deforms from the folded to the unfolded configuration. We address the mechanism of transformation from one mode shape to another using a reduced four-mass model later in §3c(ii).

Let us now examine the displacement when a lattice with a higher stiffness parameter value $\gamma = 0.2$ is subjected to a similar tensile strain. Figure 7d displays the vertical displacement of the interior nodes (z_2–z_9) as it deforms from the folded to the unfolded configuration. In contrast to the low-stiffness-parameter case, here the vertical displacement remains zero for larger tensile strains until around $\delta = -0.1$, when the vertical displacement jumps sharply to a non-zero value. The vertical displacement of the adjacent nodes has opposite sign and resembles the second mode shape discussed above. As the tensile strain increases, the vertical displacement decreases and reaches zero at around $\delta = -0.044$. Beyond this point, the vertical displacement remains zero and the axial displacement is affine, with equal compressive strain in each of the axial springs.

(b) Linear stability analysis

To investigate the local stability of the equilibria computed above, we need to look at the Hessian H of the energy $E(X)$, in (3.1). For a chain having N masses it can be expressed as

$$H = I_N \otimes \begin{pmatrix} 0 & 0 \\ 0 & \gamma \end{pmatrix} + \sum_{p=1}^{N-1} K_{h,p}, \tag{3.2}$$

where I_N is the $N \times N$ identity matrix and $\otimes$ denotes the tensor product. Here $K_{h,p}$ is the contribution due to the pth axial spring having a deformed length r_p, with an angle θ_p with respect to the horizontal axis (figure 5). It can be written as

$$K_h = \mathbf{D}_p \otimes (R_p K_{\text{loc},p} R_p^{\mathsf{T}}), \tag{3.3}$$

where $\mathbf{D}_p$ is an $N \times N$ matrix with all 0 entries except for the $(p, p+1)$ principal minor,

$$\mathbf{D}_p = \begin{matrix} \\ \\ p \\ p+1 \\ \\ \\ \end{matrix} \begin{pmatrix} 0 & \cdots & \cdots & \cdots & \cdots & 0 \\ \vdots & \ddots & & & \vdots & \vdots \\ 0 & \cdots & 1 & -1 & \cdots & 0 \\ 0 & \cdots & -1 & 1 & \cdots & 0 \\ \vdots & \vdots & & \ddots & & \vdots \\ 0 & \cdots & \cdots & \cdots & \cdots & 0 \end{pmatrix},$$

while R_p is the rotation of angle θ_p and $K_{\text{loc},p}$ is related to the stiffness of the axial spring in the local coordinate system aligned with the spring axis:

$$R_p = \begin{pmatrix} \cos\theta_p & -\sin\theta_p \\ \sin\theta_p & \cos\theta_p \end{pmatrix} \quad \text{and} \quad K_{\text{loc},p} = \begin{pmatrix} 1 & 0 \\ 0 & 1 - \dfrac{1}{r_p} \end{pmatrix}. \tag{3.4}$$

It is easy to observe that if all the springs are horizontal, that is $\theta_p = 0$ or π for every p, then the x and the z parts of the Hessian H decouple. More precisely, let $\mathbf{P}$ be the permutation matrix that

sends $\mathbf{X}$ to $\widetilde{\mathbf{X}} = (x_1, x_2, \ldots, x_N, z_1, z_2, \ldots, z_N) = (X, Z)$; then we get

$$\tilde{H} = \mathbf{PHP}^{\mathrm{T}} = \begin{pmatrix} H_x & 0 \\ 0 & H_z \end{pmatrix}.$$

Moreover, one can verify that the x part of the Hessian H_x is always positive definite. Thus to analyse the stability of an equilibrium with no displacement in the z-direction, we just need to look at the eigenvalues of H_z.

Let us consider a lattice compressed from its initial unfolded configuration to a strain δ. The affine deformation induced by such a strain is given by $x_p = (1 + \delta)p$ and $z_p = 0$ for all p. This is clearly an equilibrium configuration. Since the first and last mass are fixed, the stability of this configuration is controlled by the eigenvalues of the $(N - 2) \times (N - 2)$ matrix

$$H_z^u = \begin{matrix} & \begin{matrix} 2 & 3 & & & N-2 \end{matrix} \\ \begin{matrix} 2 \\ 3 \\ \vdots \\ N-3 \\ N-2 \end{matrix} & \begin{pmatrix} \alpha & \zeta & 0 & \cdots & 0 \\ \zeta & \alpha & \zeta & \cdots & 0 \\ \ddots & \ddots & \ddots & & \vdots \\ 0 & \cdots & \zeta & \alpha & \zeta \\ 0 & \cdots & 0 & \zeta & \alpha \end{pmatrix} \end{matrix}, \tag{3.5}$$

where

$$\alpha = \gamma + \frac{2\delta}{1 + \delta} \quad \text{and} \quad \zeta = -\frac{\delta}{1 + \delta}. \tag{3.6}$$

By looking for eigenvectors X_p of the form $X_{p,q} = \sin(\omega_p(q - 1))$, $q = 2, \ldots, N - 1$, one immediately gets $\omega_p = \pi p/(N - 1)$ with associated eigenvalue

$$\lambda_p = \gamma + \frac{2\delta}{1 + \delta}(1 - \cos(\omega_p))$$

and $p = 1, \ldots, N - 2$. Thus, at the critical strain

$$\delta_u^* = \frac{-\gamma}{\gamma + 2(1 - \cos(\omega_{N-2}))},$$

λ_{N-2} becomes negative and the affine configuration loses stability. The associated mode shape is given by

$$X_{N-2,q} = \sin\left(\frac{(N - 2)(q - 1)\pi}{N - 1}\right).$$

This shows a maximum value at the centre which explains the high deformation, which leads to subsequent folding at the centre. The strain value and mode shape predicted by the above stability analysis are in excellent agreement with the numerical solution.

Let us now consider what happens when a folded lattice is stretched. The folded reference configuration is given by $z_p = 0$ for all p while $x_p = p - 1$ if $p \leq N/2$ and $x_p = p - 3$ if $p > N/2$. Thus, the strain of this configuration is $\delta = -2/(N - 1)$. If we stretch this configuration and look for an equilibrium still having $z_p = 0$ for all p, we need all springs but the central folded one to have the same strain Δ while the central one has strain $-\Delta$. We thus get $x_p = (p - 1)(1 + \Delta)$ if $p \leq N/2$ while $x_p = (p - 2)(1 + \Delta) - (1 - \Delta)$ if $p > N/2$. The total strain δ of this configuration is thus $\delta = \Delta - 2/(N - 1)$. Again we want the critical value of Δ, and thus δ, for which this configuration loses stability.

The Hessian H_z^f in this configuration is similar to (3.5), that is,

$$H_z^f = \begin{pmatrix} \alpha_2 & \zeta_2 & 0 & \cdots & & 0 \\ \zeta_2 & \alpha_3 & \zeta_3 & \cdots & & 0 \\ \vdots & \ddots & \ddots & \ddots & & \vdots \\ 0 & \cdots & \zeta_{N-3} & \alpha_{N-2} & \zeta_{N-2} \\ 0 & \cdots & 0 & \zeta_{N-2} & \alpha_{N-1} \end{pmatrix}, \tag{3.7}$$

where

$$\alpha_p = \gamma + \frac{2\Delta}{1 + \Delta} \quad \text{and} \quad \zeta_p = -\frac{\Delta}{1 + \Delta},$$

for all p except for

$$\alpha_{N/2} = \alpha_{N/2+1} = \gamma + \frac{\Delta}{1 + \Delta} - \frac{\Delta}{1 - \Delta} \quad \text{and} \quad \zeta_{N/2} = \frac{\Delta}{1 - \Delta}.$$

Let $\mathbf{Q}$ be the reflection matrix such that $(\mathbf{Q}X)_p = X_{N-p}$. Clearly, $\mathbf{H}_z^f$ commutes with $\mathbf{Q}$ so that we know all eigenvectors X of $\mathbf{H}_z^f$ must satisfy $\mathbf{Q}X = \pm X$. This means that they are either symmetric or anti-symmetric with respect to the reflection $p \to N - p$. Taking this into consideration, we find that the search for the eigenvalues of $\mathbf{H}_z^f$ can be reduced to that of the eigenvalues of the two $(N/2 - 1) \times (N/2 - 1)$ matrices given by

$$\mathbf{H}_\pm = \begin{pmatrix} \alpha & \zeta & & & \\ \zeta & \alpha & \zeta & 0 & \\ & & \ddots & & \\ & 0 & & \alpha & \zeta \\ & & & \zeta & \beta_\pm \end{pmatrix}, \tag{3.8}$$

where

$$\alpha = \gamma + \frac{2\Delta}{1 + \Delta}, \quad \zeta = -\frac{\Delta}{1 + \Delta} \tag{3.9}$$

and

$$\beta_+ = \gamma + \frac{\Delta}{1 + \Delta} \quad \text{and} \quad \beta_- = \gamma + \frac{\Delta}{1 + \Delta} - \frac{2\Delta}{1 - \Delta}.$$

Here β_+ refers to the symmetric eigenvalues while β_- to the anti-symmetric ones.

As before, it is natural to look for eigenvectors X_p of the form $X_{p,q} = \sin(\omega_p(q - 1))$, $q = 2, \ldots, N/2 - 1$. This leads to the condition

$$(\beta_\pm - \alpha) \sin(\omega M) = \zeta \sin(\omega(M + 1)),$$

where $M = N/2 - 1$.

In the symmetric case this reduces to

$$\sin(\omega M) = \sin(\omega(M + 1))$$

so that we get the solutions $\omega_p = \pi p/(2M + 1)$ with eigenvalue $\lambda_p = \alpha + 2\gamma \cos(\omega_p)$. It is easy to see that these eigenvalues are always positive for $\Delta > 0$. In the anti-symmetric case, we get

$$\sin(\omega(M + 1)) = \frac{3 + \Delta}{1 - \Delta} \sin(\omega M). \tag{3.10}$$

Observe that since

$$\frac{3 + \Delta}{1 - \Delta} > \frac{M + 1}{M},$$

then (3.10) admits also exactly one complex solution $\omega_r = i\nu^r$. The associated eigenvector is thus $X_q^r = \sinh \nu^r(q - 1)$ with eigenvalue $\lambda^r = \alpha + 2\gamma \cosh(\nu^r)$. A complete basis of eigenvectors is then obtained from the real solution of (3.10). It is not hard to see that if ω is real than the associated eigenvalue is positive for $\Delta > 0$.
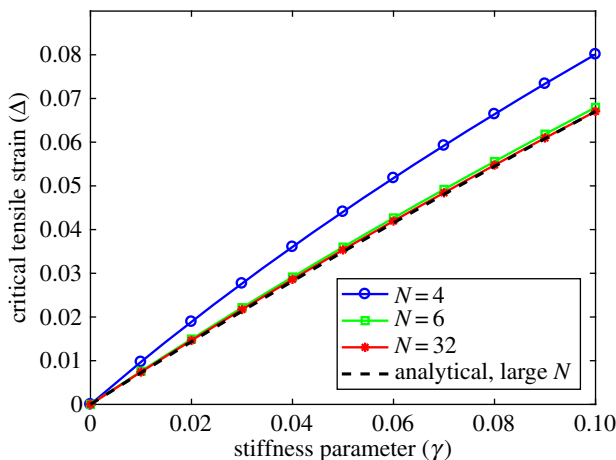
Figure 8. Tensile strain in the axial spring with stiffness parameter γ at the onset of unfolding for three different chain lengths. A chain of six masses can essentially capture the onset of bifurcation from the folded configuration of a much larger chain with reasonable accuracy. (Online version in colour.)

It is not easy to give an exact expression for ν^r for finite r. If we take the limit $M \to \infty$ and assume that ν^r has a limit, we obtain, after some algebra,

$$\cosh(\nu^r) = \frac{1}{2}\left(\frac{3+\Delta}{1-\Delta} + \frac{1-\Delta}{3+\Delta}\right) = \frac{5+2\Delta+\Delta^2}{3-2\Delta-\Delta^2},$$

so that

$$\lambda^r = \frac{(\gamma+4)\Delta^2 + 2(\gamma+2)\Delta - 3\gamma}{\Delta^2 + 2\Delta - 3}.$$

We thus obtain that the critical strain at which the folded configuration loses stability is given by

$$\Delta^* = \frac{-(\gamma+2) \pm 2\sqrt{(\gamma+2)^2 - 3}}{\gamma+4}. \tag{3.11}$$

To evaluate how close the above asymptotic value of Δ^* is to the real value for finite N, we computed Δ^* numerically. Since the eigenvalues of $\boldsymbol{H}_-$ in (3.8) are distinct, only one can become zero at the onset of the instability and thus the stability of this configuration can be evaluated by simply examining the sign of the determinant of the matrix $\boldsymbol{H}$.

Figure 8 displays the critical tensile strain Δ^* at the onset of the unfolding bifurcation transition for a range of stiffness parameter values. Three distinct chain lengths are considered, with $N = 4, 6$ and 32 point masses. In each case, the critical spring length increases almost linearly with the stiffness parameter γ. Furthermore, this critical value in a finite chain converges rapidly to the corresponding value in an infinite chain. Indeed, the critical strain in a chain with six masses is quite close to that in the 32-mass chain.

(c) Unfolded to folded transitions

Having clarified the folding transition and identified the onset of bifurcation points using a stability analysis, let us now turn attention to analysing the transition path between the two zero-energy configurations. We use two numerical techniques for this purpose. We first use a standard shooting method-based procedure to investigate this localizing transition in detail in §3c(i). We use this method to illustrate the stability regions as γ increases and the associated hysteretic behaviour. For a moderate number of masses, 10 in our present study, we found this approach hereafter outlined useful in understanding the bifurcation structure. We are aware that

this approach may have limitations for a large number of masses. We then use a classical arc-length solver-based continuation scheme in §3c(ii) on a further simplified four-mass chain which confirms the folding transition.

(i) Shooting method for 10-mass chain

Here we cast the governing equations for the equilibria into the evolution of a dynamical system. Note that the governing equation of an interior node p depends only on its nodal location and the location of its nearest-neighbour nodes ($p-1$ and $p+1$). The governing equations may be used to solve for the nodal location of the $p+1$ node if the other two nodal locations are provided. Accordingly, we may write a relation of the form

$$x_{p+1} = f(x_p, x_{p-1}), \tag{3.12}$$

where $x_p = (x_p, z_p)$. To determine explicit expressions for x_{p+1} above, as before we let $x_{p+1} - x_p = r_p \cos\theta_p$ and $z_{p+1} - z_p = r_p \sin\theta_p$. Figure 5 displays a schematic of a part of the chain with the relevant variables.

With this set-up, the equilibrium equations for the mass p, obtained by resolving the forces due to the springs in the horizontal and vertical directions, may be written as

$$(r_p - 1)\cos\theta_p = (r_{p-1} - 1)\cos\theta_{p-1} \tag{3.13a}$$

and

$$(r_p - 1)\sin\theta_p = (r_{p-1} - 1)\sin\theta_{p-1} + \gamma z_p. \tag{3.13b}$$

These equations can be unambiguously solved to obtain r_p and θ_p as functions of x_{p-1} and x_p. An explicit formula for x_{p+1} is then easily obtained using

$$x_{p+1} = x_p + r_p\cos\theta_p \quad \text{and} \quad z_{p+1} = z_p + r_p\sin\theta_p. \tag{3.14}$$

As discussed in §3b, the onset of instability for both the folded and unfolded configurations happens along an anti-symmetric mode shape with respect to the reflection $\mathbf{Q}$; see discussion after (3.7). We thus expect that the deformation process from the unfolded to the folded configuration will pass only through anti-symmetric configurations, that is configurations for which $x_{10} - x_{10-p} = x_p$ and $z_{10-p} = -z_p$. This is well verified in figure 7.

To find an equilibrium configuration for the chain, we first fix x_5 and as a consequence x_6. Observe that, due to the symmetry of the configuration, this is equivalent to fixing θ_5 and r_5 which from now on we will call θ and r. Once x_5 and x_6 are fixed, we can use (3.12) to compute x_7 up to x_{10} and as a consequence we get a full configuration for the chain.

At this point, there is no need for z_{10} to be 0. For a range of values of r, we search for the value of θ for which $z_{10} = 0$. Finally, we relate back x_{10} to the strain δ. We call this procedure the *shooting method* to find numerically an equilibrium configuration. Observe that high iterations of f in (3.12) potentially present stability issues. This is the reason why we decided to compute only anti-symmetric configurations starting from the centre of the chain. This is also the reason why the application of this method to longer chains may require a more refined analysis of the dynamical system generated by f.

To gain further insight into the difference between the high- and low-stiffness-parameter responses (figure 7) and to understand the displacement jump in figure 7d, let us examine the solution as the centre spring folds. Figure 9a displays the vertical displacement of the centre mass z_5 with compressive strain δ for four distinct stiffness parameter values. These curves are obtained from the shooting method solution described above. For low γ, there is a single solution for each strain value in the range $\delta \in [-\frac{2}{9}, 0]$. However, as the stiffness parameter γ increases, there are three possible solutions in a range of δ values. This multiplicity of solutions is evident as the curve bends backwards yielding two stable and one unstable solution for each δ value. By comparison, in figure 9b we show with black circles the stable solution computed with the previously described Newton–Raphson approach, as the lattice is stretched from the folded to the unfolded configuration. Obviously, there is an excellent agreement with the shooting method
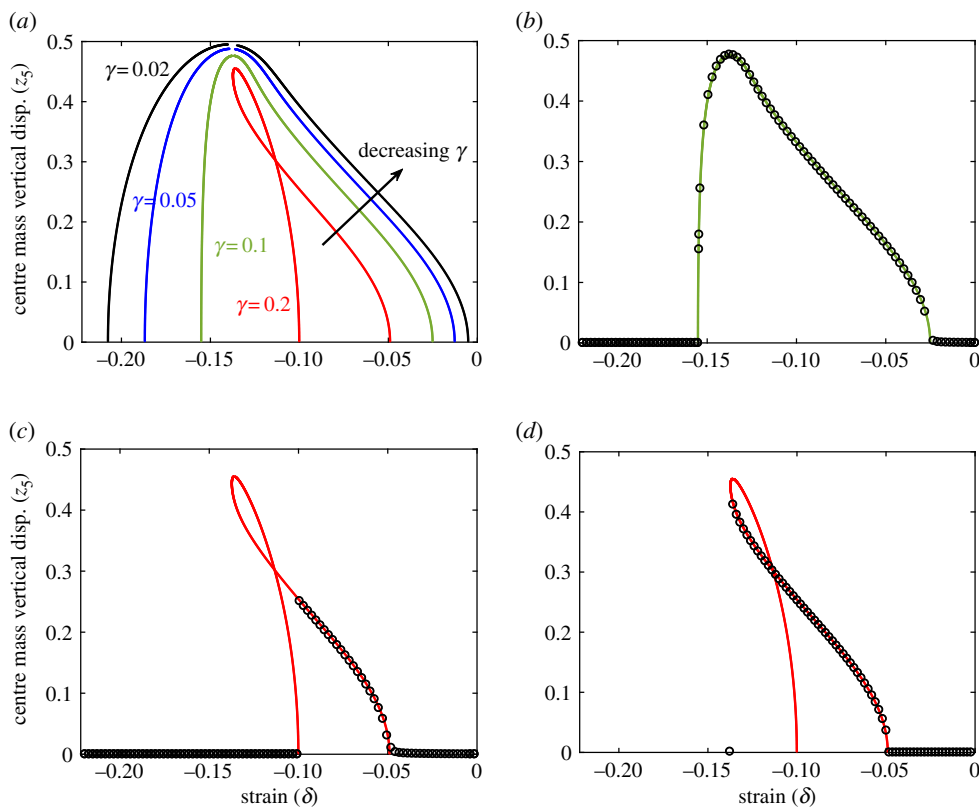
14

rsta.royalsocietypublishing.org *Phil. Trans. R. Soc. A* **376**: 20170140

Figure 9. (*a*) Vertical displacement of the centre mass with the axial position of the last mass during the folding process for different stiffness parameter γ values. The Newton–Raphson method solution (black circles) matches the shooting method solution (curves) in both loading and unloading for $\gamma = 0.1$ (*a*,*b*), while the displacement jumps after the onset of instability in both loading (*c*) and unloading (*d*) for $\gamma = 0.2$. (Online version in colour.)

solution (solid curve) over the entire range of the folding to unfolding transition. Furthermore, the Newton–Raphson method solution of lattice compression from the unfolded to the folded configuration also matches with this solution.

Let us now examine the response of a lattice having a higher stiffness parameter ($\gamma = 0.2$). Figure 9*c* displays the Newton–Raphson method solution (black circles) as this lattice is stretched from the folded to the unfolded configuration. As we discussed earlier, the solution is unstable for high θ values and our Newton–Raphson method solution jumps to a stable branch, which corresponds to a lower θ value. As the displacement increases, the solution follows this branch until $\theta = 0$ at around $\delta = -0.049$ after which the vertical displacement of all the nodes is zero. Finally, let us observe the behaviour of this lattice as it is compressed to deform from the unfolded to the folded configuration. Figure 9*d* displays the Newton–Raphson method solution for this case. The Newton–Raphson method solution matches with the shooting method solution until the onset of instability, when the tangent to the red curve in the figure becomes vertical. Beyond this point, our Newton–Raphson solver fails to converge to a stable equilibrium solution. The black circle at around $\delta = -0.138$ indicates the stable solution which a physical system is likely to reach as the prescribed compressive strain increases, which corresponds to a folded configuration, and then follows this horizontal branch (coinciding with the previous unfolding case). Thus, we observe how the solution can be path-dependent for high stiffness parameter γ values when there are multiple stable solutions.
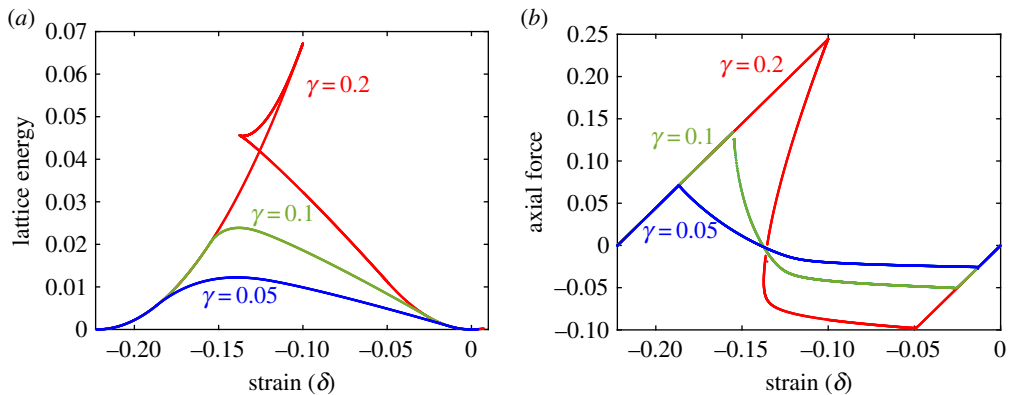
Figure 10. (a) Lattice energy and (b) force acting on the ends of the lattice as it deforms for different stiffness parameter values. As the stiffness increases, the force is not unique in a range of displacements and allows for hysteresis during the folding process. (Online version in colour.)

Having provided evidence for the existence of multiple stable solutions, let us see how the lattice energy and force vary as the lattice deforms from one equilibrium configuration to another. Figure 10a displays the lattice energy in the vertical axis as it deforms from the folded to the unfolded configuration. The strain δ on the horizontal axis ranges from $-\frac{2}{9} \simeq -0.22$ to 0. Three curves corresponding to distinct values of stiffness parameter γ are shown. In each case, the lattice energy is zero at both the folded and unfolded configurations, resulting in a double-well potential in this range of deformations. At low γ values, there is a single energy value for each strain δ, while at high γ, there are multiple energy values consistent with the observations above. For $\gamma = 0.2$, we observe that the energy curve has three segments and folds back at around $\delta = -0.138$ and -0.1. The middle segment joining the two end segments corresponds to the unstable branch.

Let us now illustrate how the corresponding horizontal force F acting on the chain varies during the folding process. It is defined as the derivative of the potential energy with respect to the chain length, given by

$$F = \frac{1}{N-1} \frac{\partial E}{\partial \delta},$$

and it is computed by taking the numerical derivative of the energy illustrated in figure 10a. Figure 10b illustrates the force for the same three stiffness parameter values γ. In all cases, the force is zero in the folded and unfolded configurations at $\delta = -\frac{2}{9}$ and $\delta = 0$. For low stiffness parameter values ($\gamma = 0.05$ and $\gamma = 0.1$ in the figure), there is again a unique force for each strain value δ. The force–displacement response has three segments: two linear and one segment in the middle joining them. The linear segments correspond to affine horizontal deformation about the folded and unfolded configurations. The middle segment corresponds to the rotation of the centre spring as θ varies from 0 to π and the effective stiffness of the chain is negative in this regime as the force decreases with increasing prescribed displacement or tensile strain. Furthermore, there are multiple values of force in a range of strains δ for the $\gamma = 0.2$ high-stiffness-parameter case. In this range of displacements, there are two stable solutions and one unstable branch. The force–displacement response illustrates the potential for achieving hysteresis in our lattice in two ways. By prescribing displacement and alternating between the folded and unfolded configurations in a lattice with high stiffness parameter γ, the lattice follows a different path around the unstable branch. For example, in figure 10b, the force jumps down from 0.24 to -0.088 while unfolding and it jumps up from -0.042 to 0.17 while folding.

Remark 3.1. We briefly remark on the alternative possibility of inducing hysteresis by exploiting the negative stiffness zone. Instead of prescribing displacement, if we prescribe a horizontal force at the ends of the chain, then the lattice solution will jump at the end of the
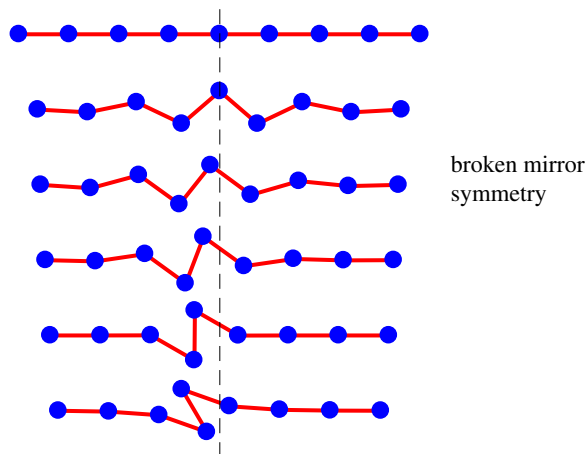
Figure 11. Deformation sequence for a chain with odd number of masses, showing an additional breaking of mirror symmetry about the chain centre, during the transition from diffuse to localized deformation. (Online version in colour.)

first segment for all three stiffness values, for example at a force level $F = -0.026$ from $\delta = -0.013$ while folding and at a force level $F = 0.0710$ from $\delta = -0.187$ while unfolding. Thus, our results illustrate the potential for hysteresis and localization guided programmable smart materials in lattice-based media.

Remark 3.2. Finally, we remark on the behaviour of a chain with an odd number of masses. Our preliminary investigations showed that such chains behave differently, although they exhibit similar folding transitions. The difference arises due to an additional breaking of mirror symmetry, as illustrated in figure 11.

(ii) Arc-length method for four-mass chain

Here we consider the simplest case of $N = 4$, that is a chain of four point masses anchored at its extremes. As in previous sections, the unfolded and folded configurations of the four masses are

$$(0,0), \ (1,0), \ (2,0), \ (3,0) \quad \text{and} \quad (0,0), \ (1,0), \ (0,0), \ (1,0).$$

We can (and will) parametrize the x-coordinate of the last mass as $3l$, with $\frac{1}{3} \leq l \leq 1$, ranging through the folded and unfolded states. Alternatively, we can use the strain, which is related to l by the linear relation

$$\delta = l - 1 \in [-\tfrac{2}{3}, 0].$$

Calling $x_i = (x_i, z_i)$ the position of the ith point mass, the energy of the system, expressed in non-dimensional form by normalizing it by a reference energy $k_0 a^2/2$, is

$$E = \frac{\gamma}{2} \sum_{i=1}^{4} z_i^2 + \frac{1}{2} \sum_{i=1}^{3} (\|x_{i+1} - x_i\| - 1)^2, \tag{3.15}$$

where the first sum is the potential energy of the vertical restoring force and the last sum is the potential energy of the springs. In this last sum x_1 and x_4 represent the fixed extremes of the chain, namely $x_1 = (0,0)$ and $x_4 = (3l,0)$.

Now, with $N = 4$, we assume that the equilibrium position satisfies $x_3 = 3l - x_2$ and $z_3 = -z_2$. Let us call r the length of the segment from the middle point to the location of the second point mass x_2, and call θ the angle formed between the middle point and the horizontal. This way, the
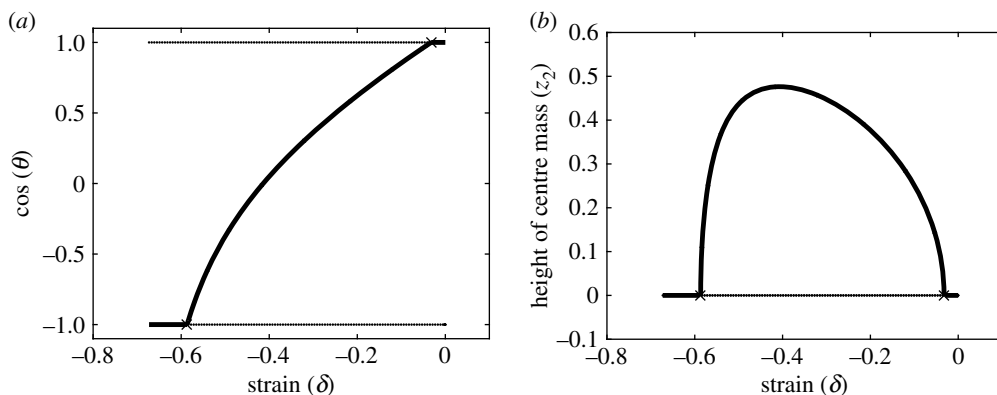
Figure 12. $\gamma = 0.1$. Stable equilibria connection between unfolded and folded configurations.

four point masses get located at the points

$$x_1 = (0,0), \quad x_2 = \left(\tfrac{3l}{2} - r\cos\theta, \, r\sin\theta\right), \quad x_3 = \left(\tfrac{3l}{2} + r\cos\theta, \, -r\sin\theta\right) \quad \text{and} \quad x_4 = (3l, 0).$$

Clearly, we have only the variables r and θ to consider and the potential to minimize becomes

$$E(r,\theta) = \gamma r^2 \sin^2\theta + \left(\sqrt{r^2 - 3lr\cos\theta + \frac{9l^2}{4}} - 1\right)^2 + \frac{1}{2}(2r - 1)^2,$$

so that by taking derivatives we get the necessary conditions

$$\left.\begin{aligned}
E_r &\equiv 2\gamma r\sin^2\theta + (2r - 3l\cos\theta)\left(1 - \left(r^2 - 3lr\cos\theta + \frac{9l^2}{4}\right)^{-1/2}\right) + 2(2r - 1) = 0 \\[2mm]
\text{and} \quad E_\theta &\equiv 2\gamma r^2\sin\theta\cos\theta + 3lr\sin\theta\left(1 - \left(r^2 - 3lr\cos\theta + \frac{9l^2}{4}\right)^{-1/2}\right) = 0.
\end{aligned}\right\} \quad (3.16)$$

Now, observe that there are two solutions valid for all γ:

Unfolded $r = l/2$ and $\theta = 0$;
Folded $\quad r = \tfrac{2}{3} - l/2$ and $\theta = \pi$.

Unlike our previous numerical experiments, here we implement a classic pseudo-arc-length continuation algorithm starting with the trivial solution branch $(l/2, 0)$ for l ranging from $l = 1$ to $l = \tfrac{1}{3}$, and monitoring branch points[1] originating from this branch. Further following this bifurcating branch, we will eventually connect the branch $(l/2, 0)$ to the other solution branch $(\tfrac{2}{3} - l/2, \pi)$. Stability monitoring is done by looking at the Hessian eigenvalues. In figures 12–14, we show what happens for several different values of γ. The most insightful visualizations are obtained displaying the values of $\cos(\theta)$, with the two trivial branches corresponding to the values 1 and −1; when not confusing, we also display the height value, as in the figures of the previous sections. We will show in thick lines the stable portions of the equilibrium branches. In spite of different values of γ, the picture we obtain in this simple case of $N = 4$ is quite similar to what we observed in the previous sections for $N = 10$.

For γ small ($\gamma = 0.1$ in figure 12), we have a stable connection of equilibrium configurations between the two trivial branches of equilibria. That is, for each value of the strain in $[-\tfrac{2}{3}, 0]$, there is always only one stable stationary solution.

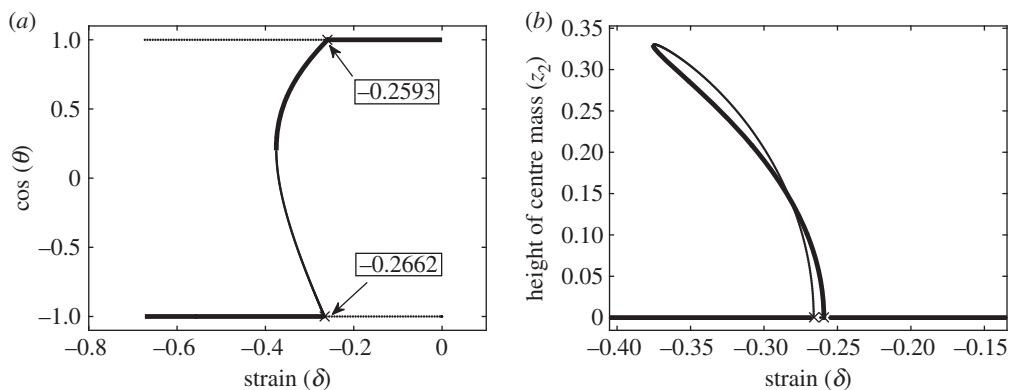[1]Namely, values where there is another solution branch passing through them.

Figure 13. Partially stable equilibria connection between unfolded and folded configurations. Hysteretic behaviour.
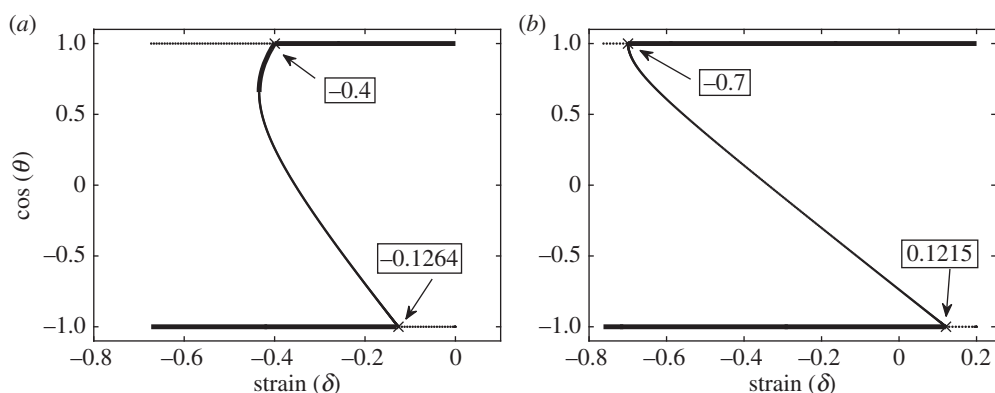

Figure 14. (a) $\gamma = 2$. Both folded and unfolded branches are stable for a range of strain values. (b) $\gamma = 7$. As γ becomes large, the branch of equilibria connecting folded and unfolded states is fully unstable; the states themselves are stable for all strain values.

As γ grows, the stable connection between the two trivial branches develops a fold and there are two stable equilibrium solutions for a range of values of the strain: one of the trivial branches and (a portion of) the connecting branch; see the case of $\gamma = 1.05$ in figure 13.

At the same time, as we increase γ further, there is a range of values of the strain where both trivial branches are stable, as well as part of the connecting branch of equilibria; see $\gamma = 2$ in figure 14a. Eventually, for γ sufficiently large ($\gamma = 7$ in figure 14b), the connecting branch is made up entirely of unstable equilibria and the branch points on the trivial branches occur outside the range of values of the unfolded/folded configurations.

Remark 3.3. As an alternative to the continuation technique we used, we also double-checked our results by a more algebraic technique, obtaining the same results. Dividing the second equation in (3.16) by $r \sin \theta$, and with some algebra, (3.16) can be rewritten as

$$\left. \begin{aligned} (2\gamma r \cos\theta + 3l)^2 \left(r^2 - 3lr\cos\theta + \frac{9l^2}{4} \right) = 9l^2 \\ (2r - 3l\cos\theta)\gamma r\cos\theta - 3l(\gamma r\sin^2\theta + 2r - 1) = 0. \end{aligned} \right\} \tag{3.17}$$

and

From (3.17), the second equation becomes

$$2\gamma r^2 \cos\theta - 3l((\gamma + 2)r - 1) = 0,$$

19

rsta.royalsocietypublishing.org *Phil. Trans. R. Soc. A* **376**: 20170140

that is,

$$\cos\theta = \frac{3l((\gamma+2)r-1)}{2\gamma r^2},\tag{3.18}$$

which, replaced in the first of (3.17), gives

$$(3l((\gamma+2)r-1)+3lr)^2(8\gamma r^3 - 36l^2((\gamma+2)r-1)+18\gamma l^2 r) - 72\gamma l^2 r^3 = 0$$

or

$$18l^2 - 9l^2(5\gamma+16)r + 18l^2(\gamma+3)(2\gamma+7)r^2 - 9l^2(\gamma+3)^2(\gamma+4)r^3$$
$$- 8\gamma(\gamma+3)r^4 + 4\gamma(\gamma+3)^2 r^5 = 0.$$

From the roots of this quintic, which we get by finding them as eigenvalues of the associated companion matrix (and keeping only the real ones for which the relative $\cos\theta$ given by (3.18) is in $[-1, 1]$), we obtain the possible equilibrium solutions.

4. Conclusion

To understand, predict and control localization patterns in lattices, we considered a square lattice on an elastic substrate. We exemplified how the type of instability changes from in-plane to out-of-plane with increasing stiffness parameter. The latter instability evolves to a localized deformation with increasing strain and it is investigated in detail using a 1D lattice. Using a shooting method-based approach, we identified the stable branches of deformation as the lattice deforms from one stable configuration to another with a localized deformation. For lattices with low stiffness parameter, there is only one stable solution as the localized pattern forms, while if this spring stiffness exceeds a critical value, there are two stable solutions in a range of displacements. The lattice energy and force response demonstrate the potential for inducing hysteresis due to the existence of the two stable solutions. Finally, we considered the simplest model possible, four point masses with the two end points fixed. In this case, we used a classical continuation technique and were able to confirm the transition from unfolded to folded quasi-static equilibrium configurations.

In summary, we have illustrated that, in contrast to many other existing works where localization is unpredictable and sensitive to the presence of defects, localized deformation can be predicted precisely based on geometry and symmetry considerations. The model presented here provides insight into the localization process and can, in principle, be extended to study thin sheets, or lattices, or an appropriate realistic system, by adding further interactions. Our analysis framework may open avenues for controlled design of interfaces for waveguiding and programmable smart materials applications.

References

1. Yoo MH. 1981 Slip, twinning, and fracture in hexagonal close-packed metals. *Metall. Trans. A* **12**, 409–418. (doi:10.1007/BF02648537)
2. Murisic N, Hakim V, Kevrekidis IG, Shvartsman SY, Audoly B. 2015 From discrete to continuum models of three-dimensional deformations in epithelial sheets. *Biophys. J.* **109**, 154–163. (doi:10.1016/j.bpj.2015.05.019)
3. Ramsay JG. 1974 Development of chevron folds. *Geol. Soc. Am. Bull.* **85**, 1741–1754. (doi:10.1130/0016-7606(1974)85<1741:DOCF>2.0.CO;2)
4. Kochmann DM, Bertoldi K. 2017 Exploiting microstructural instabilities in solids and structures: from metamaterials to structural transitions. *Appl. Mech. Rev.* **69**, 050801. (doi:10.1115/1.4037966)

5. Bhattacharya K. 2003 *Microstructure of martensite: why it forms and how it gives rise to the shape-memory effect*, vol. 2. Oxford, UK: Oxford University Press.

6. Xu F, Potier-Ferry M, Belouettar S, Hu H. 2015 Multiple bifurcations in wrinkling analysis of thin films on compliant substrates. *Int. J. Non-Linear Mech.* **76**, 203–222. (doi:10.1016/j.ijnonlinmec.2014.12.006)

7. Pocivavsek L, Dellsy R, Kern A, Johnson S, Lin B, Lee KYC, Cerda E. 2008 Stress and fold localization in thin elastic membranes. *Science* **320**, 912–916. (doi:10.1126/science.1154069)

8. Geymonat G, Müller S, Triantafyllidis N. 1993 Homogenization of nonlinearly elastic materials, microscopic bifurcation and macroscopic loss of rank-one convexity. *Arch. Ration. Mech. Anal.* **122**, 231–290. (doi:10.1007/BF00380256)

9. Kane CL, Lubensky TC. 2014 Topological boundary modes in isostatic lattices. *Nat. Phys.* **10**, 39–45. (doi:10.1038/nphys2835)

10. Anderson MS, Williams FW. 1986 Natural vibration and buckling of general periodic lattice structures. *AIAA J.* **24**, 163–169. (doi:10.2514/3.9237)

11. Paulose J, Meeussen AS, Vitelli V. 2015 Selective buckling via states of self-stress in topological metamaterials. *Proc. Natl Acad. Sci. USA* **112**, 7639–7644. (doi:10.1073/pnas.1502939112)

12. Triantafyllidis N, Schraad MW. 1998 Onset of failure in aluminum honeycombs under general in-plane loading. *J. Mech. Phys. Solids* **46**, 1089–1124. (doi:10.1016/S0022-5096(97)00060-4)

13. Hutchinson JW, Chen X. 2004 Herringbone buckling patterns of compressed thin films on compliant substrates. *J. Appl. Mech.* **71**, 597–603. (doi:10.1115/1.1756141)

14. Bertoldi K, Boyce MC. 2008 Mechanically triggered transformations of phononic band gaps in periodic elastomeric structures. *Phys. Rev. B* **77**, 052105. (doi:10.1103/PhysRevB.77.052105)

15. Pal RK, Ruzzene M, Rimoli JJ. 2016 A continuum model for nonlinear lattices under large deformations. *Int. J. Solids Struct.* **96**, 300–319. (doi:10.1016/j.ijsolstr.2016.05.020)

16. Pal RK, Rimoli JJ, Ruzzene M. 2016 Effect of large deformation pre-loads on the wave properties of hexagonal lattices. *Smart Mater. Struct.* **25**, 054010. (doi:10.1088/0964-1726/25/5/054010)

17. Lee A, Jiménez FL, Marthelot J, Hutchinson JW, Reis PM. 2016 The geometric role of precisely engineered imperfections on the critical buckling load of spherical elastic shells. *J. Appl. Mech.* **83**, 111005. (doi:10.1115/1.4034431)

18. Combescure C, Henry P, Elliott RS. 2016 Post-bifurcation and stability of a finitely strained hexagonal honeycomb subjected to equi-biaxial in-plane loading. *Int. J. Solids Struct.* **88**, 296–318. (doi:10.1016/j.ijsolstr.2016.02.016)

19. Rudnicki JW, Rice JR. 1975 Conditions for the localization of deformation in pressure-sensitive dilatant materials. *J. Mech. Phys. Solids* **23**, 371–394. (doi:10.1016/0022-5096(75)90001-0)

20. Gibson LJ, Ashby MF. 1999 *Cellular solids: structure and properties*. Cambridge, UK: Cambridge University Press.

21. Papka SD, Kyriakides S. 1994 In-plane compressive response and crushing of honeycomb. *J. Mech. Phys. Solids* **42**, 1499–1532. (doi:10.1016/0022-5096(94)90085-X)

22. Papka SD, Kyriakides S. 1998 Experiments and full-scale numerical simulations of in-plane crushing of a honeycomb. *Acta Mater.* **46**, 2765–2776. (doi:10.1016/S1359-6454(97)00453-9)

23. Papka SD, Kyriakides S. 1999 Biaxial crushing of honeycombs:—Part 1: Experiments. *Int. J. Solids Struct.* **36**, 4367–4396. (doi:10.1016/S0020-7683(98)00224-8)

24. d'Avila MPS, Triantafyllidis N, Wen G. 2016 Localization of deformation and loss of macroscopic ellipticity in microstructured solids. *J. Mech. Phys. Solids* **97**, 275–298. (doi:10.1016/j.jmps.2016.07.009)

25. Sievers AJ, Takeno S. 1988 Intrinsic localized modes in anharmonic crystals. *Phys. Rev. Lett.* **61**, 970. (doi:10.1103/PhysRevLett.61.970)

26. Campbell DK, Flach S, Kivshar YS. 2004 Localizing energy through nonlinearity and discreteness. *Phys. Today* **57**, 43–50. (doi:10.1063/1.1650069)

27. Li B, Cao Y-P, Feng X-Q, Gao H. 2012 Mechanics of morphological instabilities and surface wrinkling in soft materials: a review. *Soft Matter* **8**, 5728–5745. (doi:10.1039/C2SM00011C)